DIAGNOSTICS FOR COLLIMATOR IRRADIATION STUDIES IN THE ADVANCED PHOTON SOURCE STORAGE RING*

J. Dooling[†], M. Borland, W. Berg, J. Calvey, G. Decker, L. Emery, K. Harkay, R. Lindberg,
G. Navrotksi, V. Sajaev, J. Stevens, Y. P. Sun, K. P. Wootton, A. Xiao,
Argonne National Laboratory, Lemont, USA
A. H. Lumpkin, Argonne Associate of Global Empire, LLC,
Argonne National Laboratory, Lemont, USA

Abstract

The Advanced Photon Source (APS) is building a fourth-generation storage ring (4GSR), replacing the present double-bend achromat lattice with a multibend achromat system thereby allowing the production of ultra-bright x-ray beams. The new lattice enables a two-order-of-magnitude reduction in horizontal beam emittance and a factor of two increase in beam current. The result is an electron beam of very high energy- and power-densities. Initial predictions suggest virtually any material struck by the undiluted electron beam will be damaged. Two experimental beam abort studies have been conducted on collimator test pieces in the present APS SR to inform the design of a fully-functional machine protection system for APS 4GSR operations at 200 mA. A comprehensive suite of diagnostics were employed during the studies. The diagnostics used in these experiments are not new, but employed in different ways to obtain unique data sets. With these data sets now in hand, we are developing new numerical tools to guide collimator design.

INTRODUCTION

The Advanced Photon Source Upgrade (APS-U) project centers on the construction of a fourth generation storage ring (4GSR) [1]. The ultra-low emittance lattice operating at 6 GeV and 200 mA will result an electron beam of very high energy- and power-densities. MARS [2] simulations indicated virtually any material struck by the undiluted, primary beam will be damaged. The objective of this work is to conduct experimental studies which informs the design and construction of a robust, fully-functional collimator system for 200 mA APS-U beam operations. A variety of diagnostics play a key role in observing and evaluating the effects of whole beam dumps on candidate collimator materials which is the subject of these studies.

Two beam-loss studies have been performed thus far, the first in May 2019 and the second in January 2020. Conducting these experiments successfully requires a diverse set of diagnostics such as Turn-By-Turn (TBT) Beam Position Monitors (BPMs), cameras, DC Current Transformers (DC-CTs), and beam loss monitors (BLMs). A different set of diagnostic techniques are used after the study to examine the collimator test pieces including microscopy and metallurgy.

EXPERIMENTAL METHODS

Both irradiation studies were conducted at the beginning of run periods during start-up machine studies in order to extract the collimator test pieces before user operations began. This approach is somewhat risky since this time may be necessary to condition new vacuum components or other hardware; for example, the collimator/scraper assembly. A plan view of the assembly is presented in Fig. 1. This location is just downstream of the fourth rf cavity in this Sector 37 (S37) long straight section.
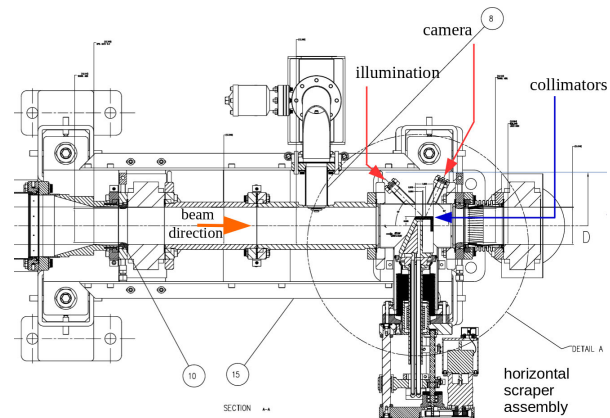

Figure 1: Collimator/scraper assembly plan view in the APS SR S37 long straight section. The location is just downstream of the fourth rf cavity.

Diagnostic Camera

For both experiments, a diagnostic camera was built in the SR tunnel to view the collimator surfaces. The camera hardware was then disassembled and removed at the end of each study. The collimators are viewed through a 65° port and illuminated through a 45° port as indicated in Fig. 1. The angles are measured from the beam axis. The depth of field (DOF) for the optical system is 2 mm at the collimator surface. The resolution is approximately 50 µm and the field of view is 11 mm. Radiation protection for the camera is provided first by moving the unit approximately 0.5 m below the beam centerline, and second by shielding with Pb bricks. A photograph of the camera assembly and image of the installed collimator pieces prior to the first irradiation experiment are shown in Fig. 2. In the first experiment, two collimator materials were tested: titanium alloy Ti6Al4V and aluminum alloy T6061. In this image the darker titanium

(a) Diagnositc Camera assembly.
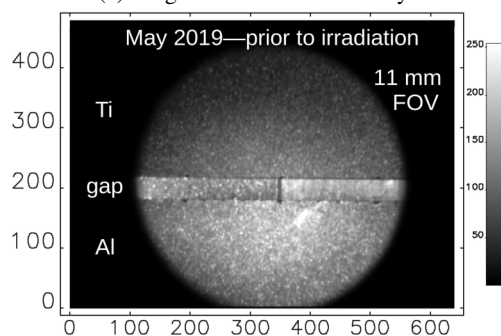
(b) Pre-Irradiation collimator image.

Figure 2: a) Diagnostic Camera hardware and b) collimator image prior to the first irradiation experiment. The field of view is approximately 11 mm and gap between collimator pieces is 1 mm.

alloy is on top; however, the image is flipped vertically so that actually the aluminum piece is above the beam centerline.

In addition to frame grabber software used to capture still images, a digital video recorder (DVR) was employed to capture images from the Diagnostic Camera during beam strikes. The DVR operated at a 30 frames per second (fps) rate with a resolution of 360 x 240. DVR playback allowed the viewing of the one video frame that had the flash of light and a 33 ms snapshot of the dynamic scene after the beam-abort trigger.

Linear Variable Differential Transformer Calibration

The position and motion of the scraper assembly needed to be accurately known for proper placement of the collimator test pieces once mounted and inside the vacuum chamber. Horizontal position placement was made using a linear variable differential transformer (LVDT). Total linear travel of the collimators was 4.747 cm. Survey and Alignment scribed the location when the collimator apex was located

at the beam centerline. The distance from a fully retracted or withdrawn position to the beam centerline was measured to be 2.774±0.005 cm.

Collimator Measurements

Two collimator test pieces are mounted on the end of the horizontal scraper shown in Fig. 1. The surface facing the beam is machined to have large radius (0.8 m) creating an apex near the center of the collimator. The apex is where we expect the beam to strike first as it loses energy after rf muting. An oblique drawing of the collimator test piece is presented in Fig. 3. The radius machined into the beam-
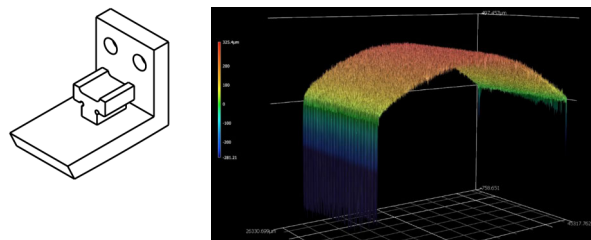
(a) Coll. test piece.   (b) Collimator surface, anamorphic view.

Figure 3: Collimator test piece a) oblique view and b) a 3000X magnification of the beam-facing surface in horizontal direction. In a), the beam-facing surface is out of view, below the image.

facing surface yields an apex approximately 0.3 mm above the chord connecting the upstream and downstream ends of the collimator. A microscope system provides both a view of the machined radius as well as surface roughness. An anamorphic image of the collimator surface magnified in the horizontal direction 3000 times is also shown in Fig. 3. The measurement was made on the aluminum test piece installed for the May 2019 experiment; the surface roughness was found to be 2.7 µm. The aluminum test pieces used in the January 2020 study had a significantly reduced surface roughness value of 0.45 µm.

Temperature and Pressure

Temperature and pressure sensors played an important role during conditioning of the collimator/scraper assembly. Temperature measurements were made with resistance temperature detectors (RTDs) and thermocouples (TCs); additional detectors were placed on the exterior of the vacuum chamber, near the beam end of the scraper. The two detectors with the highest readings from both RTDs and TCs sets are presented in Fig. 4 for the period over which all 11 200 mA beam dumps occurred. This time period occurred between two beam dumps with nominal beam currents of 150 mA. The highest readings occurred on the scraper vacuum chamber where the rf fingers are located internally, close to where the two tubes join (see Fig. 1). The number of bunches chosen for the 150 mA cases was 324 (every fourth rf bucket filled). Because of significant wakefield heating for this case, the number of bunches was increased to 972 for the 200 mA

**TUAO02**
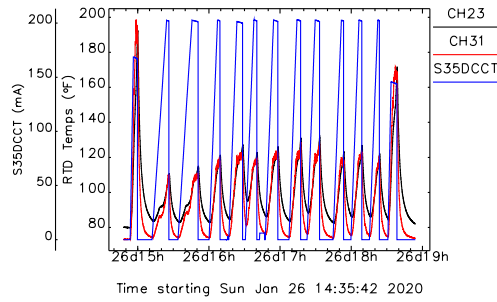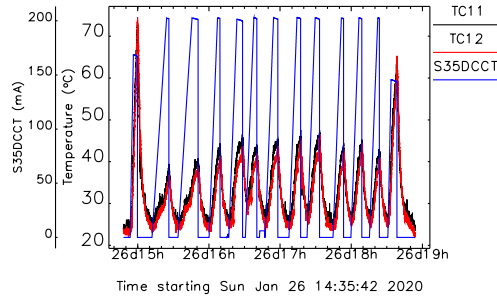
(a) RTD readings.

(b) TC readings.

Figure 4: The two highest a) RTD and b) TC readings of all nominal 200 mA beam aborts and the 150 mA cases immediately proceeding and following.

beam aborts. Wakefield heating scales approximately as MI^2 where M is the number of bunches and I is the current of a single bunch. With this scaling, the heating at 200 mA with charge spread equally over 972 bunches should be only 59% of that at 150 mA with 324 bunches.

Vacuum pressure was also of concern due to the proximity of the collimator/scraper assembly to the S37 rf cavities. Pressure in the cavities are monitored with cold cathode gauges. During conditioning on the day prior to the irradiation study, we found pressure spikes were reduced by leaving the scraper parked with the apex of the collimator surfaces 3.7 mm inboard ($x = -3.7$ mm) of the nominal beam centerline during injection. The surfaces were then moved to $x = -2.0$ mm for beam aborts. At the highest currents, modest pressure rise was observed as beam current was injected and stored for beam aborts; however, more substantial transients occurred as the beam was dumped. The collimator/scraper assembly is located 1.6 m downstream of the fourth rf cavity in the S37 long straight section. The other three cavities are located further upstream equidistantly spaced approximately 1 m apart. Figure 5 compares the the pressures recorded in the four S37 rf cavities during the first beam dump from 150 mA and a later beam abort from 200 mA. For the 150 mA case, peak pressure was recorded in chamber 4 (C4) at approximately 20 nTorr; however, at 200 mA, the peak pressure in C4 is an order of magnitude higher. As expected, peak pressures fell for cavities further away from the strike location.
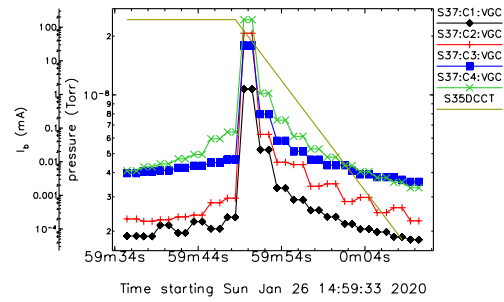
(a) 150 mA.
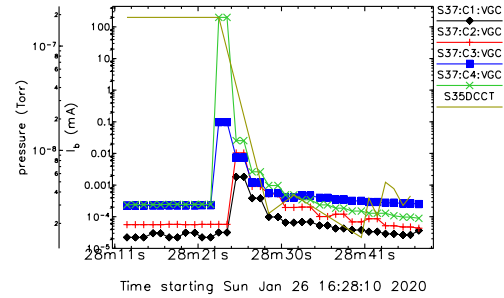
(b) 200 mA.

Figure 5: Pressure transients in the S37 rf cavities from beam dumps at a) 150 and b) 200 mA.

A pressure limit of 1 µTorr was established prior to studies as a trip level. Though exceeded during early conditioning, no trips were recorded during the collimator irradiation studies.

Gap Localization

The change of stored current with time monitored with the DCCT provides a measure of beam lifetime. Beam lifetime also allowed us to localize the center of the collimator assembly by identifying the location of the gap between the two collimator test pieces. Gap localization was accomplished by step-wise scanning a 10 mA beam vertically past the gap while measuring beam lifetime; the beam was positioned approximately 0.9 mm from the collimator surface. A sketch of the geometry and gap localization results are presented in Fig. 6.

COLLIMATOR IRRADIATION MEASUREMENTS

One of the January 2020 collimator irradiation study goals was to reach 200 mA. As mentioned above, we accomplished this goal by increasing the number of bunches from 324 to 972.

Emittance, Charge, and Current Density

Emittance is determined using a pinhole camera assuming Gaussian spatial distributions. Beam size and current density are calculated from beam emittance and lattice functions
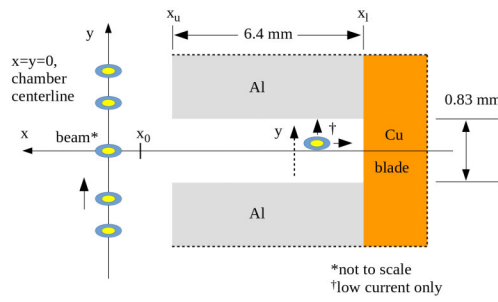
(a) Collimator gap schematic.
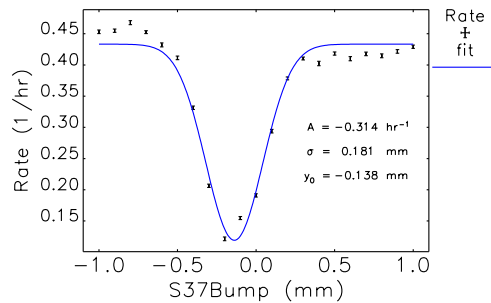
(b) Lifetime measurements.

Figure 6: a) Collimator gap geometry schematic with vertical beam scanning and b) lifetime measurements indicating the center of the gap. The beam was positioned 0.9 mm from the collimator surface.

at the scraper location assuming $\beta_x = 4.0$ m, $\beta_y = 6.0$ m, $\eta_x = 0.059$ m, $\eta_y = \eta'_x = \eta'_y = 0$, and $\Delta p/p = 10^{-3}$. The current density is calculated as $j_b = I_b/(2\pi\sigma_x\sigma_y)$. A triple reduced horizontal beamsize (RHB) lattice was developed to minimize the spot size at the S37 scraper location. The lattice was modeled with the beam dynamic code elegant [3].

Variation in vertical emittance with scraper position is observed prior to beam dumps; whereas, horizontal emittance essentially shows no change. Horizontal and vertical emittances are plotted in Fig. 7 along with scraper position for the $y_{\text{bump}} = 2.6$ mm, 200 mA beam dump case. A posi-
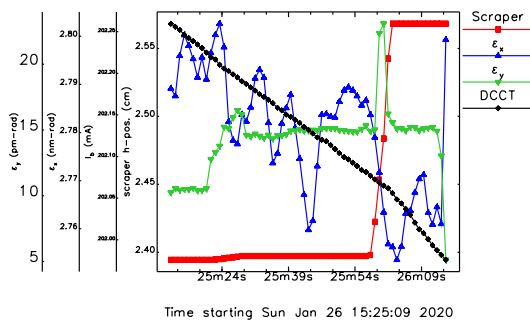

Figure 7: Beam emittances, scraper position, DCCT at 200 mA for a 2.6 mm vertical bump. Note the change in DCCT slope (reduction in lifetime) as the scraper is inserted to its final position. Also the vertical emittance transient may indicate an ion instability.

tion of 2.57 cm corresponds to the apex of the collimators at $x = -2.0$ mm from the nominal beam centerline.

Diagnostic Camera Images

Visible light emission was observed down to the lowest current levels, approximately 2 mA during the May 2019 study. At low currents, emission is likely due to scintillation or optical transition radiation; at high currents, black body radiation is dominant. During our May 2019 experiment, we were limited to maximum currents of 65 mA. Emission images from this earlier study have been previously reported [4]. The final image recorded with the diagnostic camera at the end of the study is shown in false color in Fig. 8.

Visible light emission from a pair of beam dumps from the January 2020 experiment are presented in Fig. 9. Surprisingly in our January 2020 experiment, where only aluminum test pieces were used, significantly more ejecta features were observed in the 65 mA range; see Fig. 9a. As mentioned above, the Diagnostic Camera DOF is 2 mm; therefore, the linear features seen in Fig. 9a must be close to the collimator surface. At 200 mA, the emission is much brighter while linear features, though present, are less pronounced; see Fig. 9b. The collimator surfaces are strongly affected by beam dumps; surface images and a summary of the beam dump parameters are presented in the next section.

PHOTOGRAPHY AND MICROSCOPY

Images from the May 2019 experiment showed damage to the titanium alloy test piece was significantly greater than to the aluminum for the same current [4]. Irradiation effects in titanium were observed down to 16 mA; whereas, the minimum current for surface damage in aluminum was 32 mA. One additional complication was that the titanium test piece became activated during the experiment. For these reasons, we decided not to do further testing with titanium.

In early February 2020, after the second experiment, photographs were taken of both aluminum collimator pieces while still attached to the scraper assembly; an example is presented in Fig. 10. The sequence number and times
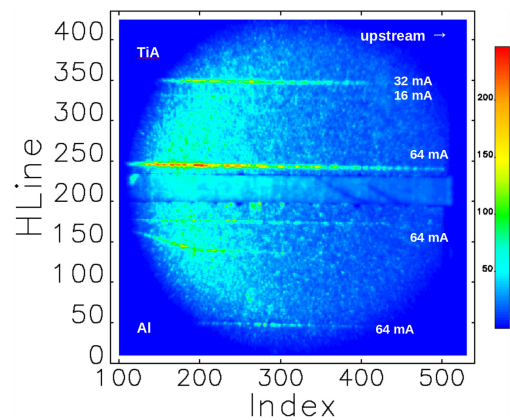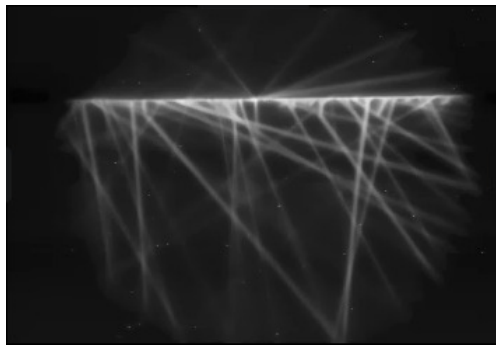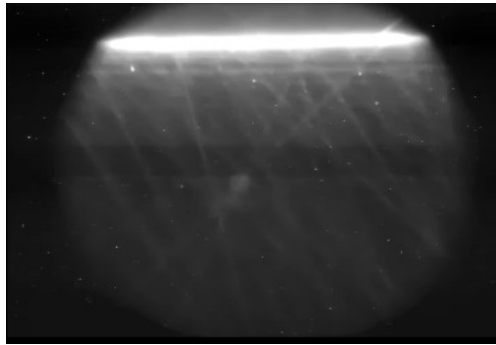

Figure 8: Last image of the collimator surfaces after the final beam dump of the May 2019 study, shown in false color.

(a) Beam strike recorded at 69.4 mA.

(b) Beam strike recorded at 201 mA.

Figure 9: Visible light emission from beam dumps at a) 69.4 mA and b) 201 mA. The beam moves from right to left.

struck are indicated on the left side of Fig. 10 while nominal current is indicated on the right side. Once the collimator pieces were removed from the scraper body, better resolution images of the irradiation surfaces were obtained.

Table 1 lists the beam dumps in sequential order along with current, emittances, rms spot sizes, and estimated dose levels. Gaussian transverse profiles are assumed. At 200 mA, calculated current densities reach 39 A mm^{-2}, approximately 5 times the damage threshold observed in aluminum. Dose
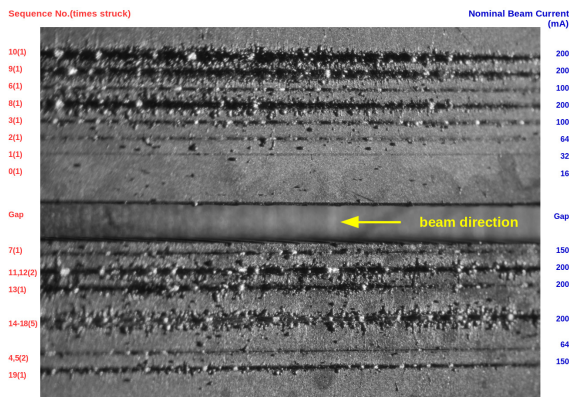

Figure 10: Higher resolution photograph of the January 2020 collimator test pieces. The pieces are still attached to the scraper body. Sequence number and times struck are shown on the left; nominal currents are listed on the right.

is calculated as,

$$D = S_{pc} \frac{N_q}{2\pi\sigma_x\sigma_y} \quad (1)$$

where S_{pc} is the collisional stopping power for 6 GeV electrons in aluminum [5] and N_q is the total number of circulating electrons. At 6 GeV, the collisional stopping power in Al is 2.153 MeV cm^2 g^{-1} (note: the radiative stopping power is 246.7 MeV cm^2 g^{-1}).

The upper collimator piece from the January 2020 study received only a single beam dump at each vertical position. Examining this piece under a microscope with different lighting orientations reveals some of the structure of the beam strike damage. Figure 11 presents a micrograph of the upper collimator piece. Starting from the bottom of the images,
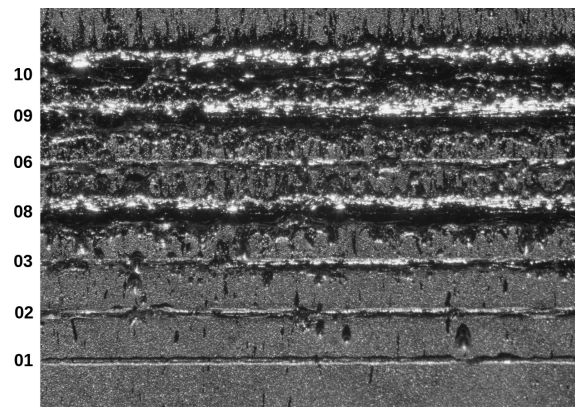

Figure 11: Microscopy image of the upper collimator piece from the January 2020 study. Starting from the bottom of the image, beam strike currents increase from 34.6 to 202.1 mA. The vertical separation between each beam strike position is 0.4 mm. Illumination is from the bottom of the image. Sequence numbers are given on the left.

the beam dump currents were 34.6, 69.4, 99.1, 202.0, 100.0, 201.2, and 202.1 mA. The nominal separation between each strike is 0.4 mm.

TURN-BY-TURN BPMS AND FAST BLMS

Beam dumps were monitored by both TBT BPMs and fast BLMs. TBT BPMs are fast enough to resolve beam position turn by turn. Fast BLMs are based on high-purity fused silica fibers as well as small cylindrical fused-silica radiators. A comparison of the differentiated TBT BPM sum signal peak times and peak loss intensity time since rf muting ("Arrival Time") from several BLMs versus current is presented in Fig. 12 for data collected during the January 2020 beam abort study. A systematic difference of approximately 2 turns (7 μs) is observed between the TBT BPMs and the fast BLM data with the fast BLM peaks appearing first. This difference may be due to the TBT BPM data being generated as the log of the sum signals, whereas the fast BLM signals are linear. Large loss signals can saturate the BLM photomultipler tubes, so care must be exercised here.

Table 1: Chronological Sequence Number (SN), No. of Bunches, Y-Offset, Beam Current, Charge per Bunch, Emittance, Spot Size, Current Density, and Dose During the January 2020 S37 Collimator Study; Gray Backgrounds Represent Locations of Repeated Beam Dumps

| SN	No. bun.	y-off. (mm)	I_b (mA)	Q_b (nC)	ϵ_x (nm)	ϵ_y (pm)	σ_x (mm)	σ_y (μm)	j_e ($\frac{A}{mm^2}$)	D (MGy)
0	27	1.0	18.1	2.18	1.831	6.00	0.1039	6.00	4.61	3.65
1	54	1.4	34.6	2.18	1.829	5.28	0.1039	5.63	9.42	7.47
2	108	1.8	69.4	2.18	1.972	7.58	0.1066	6.74	15.36	12.18
3	324	2.2	99.1	1.13	2.088	13.36	0.1088	8.95	16.20	12.84
4	108	-3.4	73.1	2.18	2.012	7.51	0.1074	6.71	16.14	12.80
5	108	-3.4	66.6	2.18	1.965	7.88	0.1065	6.88	14.47	11.47
6	324	3.0	100.0	1.13	2.023	13.74	0.1076	9.08	16.29	12.92
7	324	-1.0	166.8	1.7	2.120	9.58	0.1094	7.58	32.02	25.39
8	972	2.6	202.0	0.76	2.765	14.91	0.1206	9.46	28.18	22.35
9	972	3.4	201.2	0.76	2.094	17.85	0.1089	10.35	28.41	22.53
10	972	3.8	202.1	0.76	2.104	15.51	0.1091	9.65	30.56	24.23
11	972	-1.4	199.8	0.76	2.140	9.52	0.1097	7.56	38.33	30.39
12	972	-1.4	201.9	0.76	2.132	9.55	0.1096	7.57	38.74	30.71
13	972	-1.8	201.4	0.76	2.112	9.54	0.1092	7.57	38.79	30.76
14	972	-2.6	201.9	0.76	2.117	10.71	0.1093	8.02	36.68	29.08
15	972	-2.6	201.4	0.76	2.102	10.42	0.1090	7.91	37.18	29.48
16	972	-2.6	201.9	0.76	2.108	10.44	0.1091	7.92	37.19	29.49
17	972	-2.6	201.8	0.76	2.112	10.61	0.1092	7.98	36.86	29.22
18	972	-2.6	202.2	0.76	2.124	10.36	0.1094	7.88	37.31	29.58
19	324	-3.8	143.6	1.7	2.087	11.49	0.1088	8.30	25.32	20.07
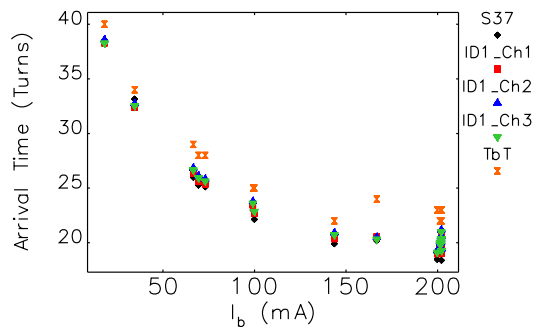
Figure 12: Comparison of arrival times of the loss signals determined from the fast BLMS and TBT BPMs.

Loss intensity signals observed on one of the fast BLMs in ID1 shows good agreement with elegant simulations. The elegant data consists of differentiated particles remaining with respect to time in Turns since rf muting. These data are plotted in Fig. 13, again from the January 2020 abort study. ID1 BLMs are 110 m downstream of the S37 scraper location.

METALLURGY

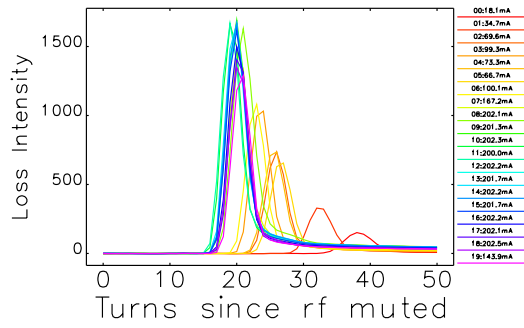Metallurgical analysis was performed on the aluminum test piece used in the May 2019 experiment. A transverse cross section was cut from the test piece, polished, then prepared with Barker's etch. A comparison of cross sections struck by 33.1 and 67.4 mA beams is presented in Fig. 14. The expansion in the affected area as the current is increased from 33.1 to 67.4 mA appears to be greater than a factor of two, especially in the partial melt zone. Based on the effects of higher current irradiation during the January 2020 experiment, these cases are viewed as being transitional from no-damage to plastic flow to melt and finally vaporization. Table 1 shows dose rates of 30 MGy were attained, a factor of 2 higher than that required for hydrodynamic behavior [6].

The reason that a metallurgical analysis of the titanium alloy piece was not conducted was its activation and the production of mixed waste cutting and polishing would have generated. After the January 2020 experiment, both of the aluminum tests pieces were found to be activated. Gamma spectroscopy conducted on March 13, 2020 showed the nuclide responsible for the largest count rate was beryllium-7. Be-7 is generated by high-energy events such as spallation or cosmic ray impacts on nitrogen or oxygen in the atmosphere.
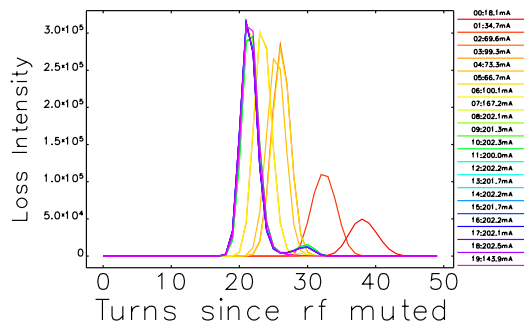
DISCUSSION

Over the range of currents and bunch patterns selected to conduct these experiments, particularly in the January study, a wide range of material behavior has been observed. Surface roughness may play a role when comparing the effects of 65 mA beam aborts in May 2019 and January 2020,

9th Int. Beam Instrum. Conf.   IBIC2020, Santos, Brazil   JACoW Publishing

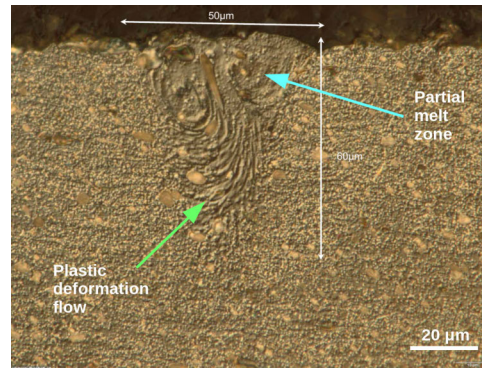ISBN: 978-3-95450-222-6   ISSN: 2673-5350   doi:10.18429/JACoW-IBIC2020-TUAO02

(a) ID1, Ch. 3 fast BLM.

(b) elegant.

Figure 13: Comparison of a) fast BLM loss intensity with b) elegant modeling for the 20 beam abort cases.

(a) 33.1 mA.

(b) 67.4 mA.

Figure 14: Cross sections of the aluminum test piece showing regions of a) 33.1 mA and b) 67.4 mA beam strikes. Regions of plastic flow and partial melt are identified. The beam direction is out of the page.
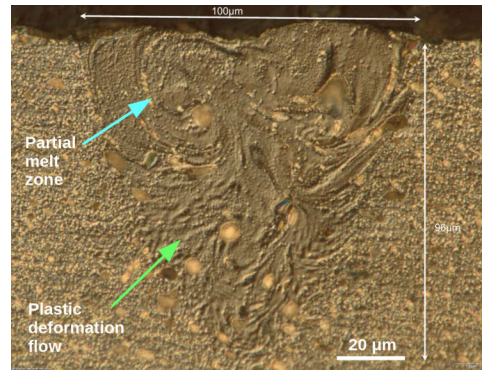
suggesting wakefield effects could be involved. However another explanations could exist such as material composition or current density. At 16 mA, no damage is detectable on the aluminum collimators; however, at 32 mA plastic deformation and partial melting take place. At 65 mA, material expulsion begins; however the transverse extent of the damage is relatively small. At 100 mA and above, the region of damage grows significantly. At 200 mA, the beam strike area is strongly evacuated leaving a clear trench even after a single dump; this is most likely a region of strong hydrodynamic activity. The large light output at high currents is ascribed as predominately black body radiation. The melting temperature of the T6061 aluminum alloy is 858 K and 2345 K for the thin aluminum oxide layer on the surface. In the May 2019 experiment, the oxide layer remained largely intact up to 65 mA; this was not the case in the January 2020 study. The fact that the heated region can be cleared in a single strike indicates the beam can propagate further downstream as it is dumped. Coupled modeling between particle-matter interaction, hydrodynamic, and beam dynamics codes (multiphysics) is required to adequately address this behavior.

SUMMARY

Two experiments have been conducted in the APS SR to reproduce expected whole-beam dump conditions in the APS-U. In the first experiment, transitions from solid to plastic/partial-melt states in Al and Ti-alloy target collimators were observed. In the second experiment, 200 mA was attained on aluminum targets; transitions to a fully hydrodynamic behavior were observed. Beam dynamics predictions by elegant show good agreement with measurements of beam arrival time and temporal pulse compression with current. Our suite of diagnostics has provided important data to allow benchmarking of coupled-code multiphysics investigations.

ACKNOWLEDGMENTS

REFERENCES

[1] M. Yabashi and H. Tanaka, "The next ten years of X-ray science", *Nature Photonics*, vol. 11, no. 1, pp. 12–14, Jan. 2017. doi:10.1038/nphoton.2016.251

[2] N. V. Mokhov et al., "MARS15 Overview", *AIP Conf. Proc.*, vol. 896, no.1, pp. 50-60, 2007. Rep. Fermilab-Conf-07/008-AD. doi:10.1063/1.2720456

[3] M. Borland, "elegant: A Flexible SDDS-Compliant Code for Accelerator Simulation", presented at the 6th International Computational Accelerator Physics Conference, ICAP2000,

Darmstadt, Germany, Sep. 2000. Rep. ANL/APS LS-287. `doi: 10.2172/761286`

[4] J. C. Dooling *et al.*, "Studies of Beam Dumps in Candidate Horizontal Collimator Materials for the Advanced Photon Source Upgrade Storage Ring", presented at the NAPAC'19, Lansing, MI, USA, Sep. 2019, paper MOPLM14.

[5] ESTAR, `https://physics.nist.gov/PhysRefData/Star/Text/ESTAR.html`

[6] D. C. Wilson, R. P. Godwin, J. C. Goldstein, N. V. Mokhov, and C. A. Wingate, "Hydrodynamic Calculations of 20-TeV Beam Interactions with the SSC Beam Dump", in *Proc. PAC'93*, Washington D.C., USA, Mar. 1993, pp. 3090–3093.